Journal of Physics D: Applied Physics

PAPER

Enhanced effective spin Hall efficiency contributed by the extrinsic spin Hall effect in $Pt_{1\text{-}x}Ta_x$/CoFeB structures

To cite this article: Zhan Xu *et al* 2024 *J. Phys. D: Appl. Phys.* **57** 145001

IOP Publishing
Journal of Physics D: Applied Physics
J. Phys. D: Appl. Phys. **57** (2024) 145001 (11pp)
https://doi.org/10.1088/1361-6463/ad1a66

Enhanced effective spin Hall efficiency contributed by the extrinsic spin Hall effect in $Pt_{1\text{-}x}Ta_x$/CoFeB structures

Zhan Xu[1,2,3,*], **Jiaxuan Tang**[4], **Sicong Hu**[3], **Er Liu**[3], **Feng Xu**[3,*], **Leixiang Bian**[1] **and Wen Siang Lew**[2,*]

[1] School of Mechanical Engineering, Nanjing University of Science and Technology, Nanjing 210094, People's Republic of China
[2] School of Physical and Mathematical Sciences, Nanyang Technological University, 21 Nanyang Link, Singapore 637371, Singapore
[3] MIIT Key Laboratory of Advanced Metallic and Intermetallic Materials Technology, School of Materials Science and Engineering, Nanjing University of Science and Technology, Nanjing 210094, People's Republic of China
[4] School of Materials Engineering, Jinling Institute of Technology, Nanjing 210094, People's Republic of China

E-mail: zhanxu@njust.edu.cn, xufeng@njust.edu.cn and wensiang@ntu.edu.sg

Received 25 November 2023, revised 25 December 2023
Accepted for publication 3 January 2024
Published 11 January 2024

Abstract

High effective spin Hall efficiency and low magnetic damping constant are essential to achieve efficient spin-charge conversion for energy-efficient spintronic devices. We report the measurements of effective spin Hall efficiency and magnetic damping constant of $Pt_{1\text{-}x}Ta_x$/CoFeB structures using spin-torque ferromagnetic resonance (ST-FMR) techniques. With the increase of Ta content, the spin Hall efficiency increases and peaks $x = 0.15$ with the value of $\theta_{SH}^{eff} = 0.35$, before decreases for further Ta content. This non-monotonic variation is attributed to the interaction between the contribution of the extrinsic skew scattering mechanism and the spin-orbit coupling (SOC). The weakening of the SOC in the $Pt_{1\text{-}x}Ta_x$ layer leads to a decrease in the effective magnetic damping constant with increasing Ta concentration. High-temperature ST-FMR measurements confirm the influence of the Ta concentration on the spin Hall effect and magnetic damping mechanism. Additionally, the decrease in spin mixing conductance and the increase in spin diffusion length leads to a decrease in the interfacial spin transparency.

Supplementary material for this article is available online

Keywords: spin Hall effect, magnetic damping, spin Hall efficiency, spin-torque ferromagnetic resonance, spin-orbit coupling

1. Introduction

The study of magnetization manipulation in heavy metal (HM)/ferromagnetic material (FM) heterostructures *via* spin-orbit torque (SOT) has attracted strong interest as there is huge potential for further development into new high-performance and energy-efficient magnetic memories, logic devices, oscillators, and non-conventional computing devices [1–5]. Furthermore, when a beam passes through an optical interface or a non-uniform medium, the photons undergo transverse spin splitting concerning the geometrical optical trajectory, called the photon spin Hall effect (SHE) [6, 7]. This effect can be considered an evolution of the SHE in electronic

* Authors to whom any correspondence should be addressed.

systems, which has a wide range of applications in precision metrology, quantum imaging, and micro-imaging [8]. In the FM/HM heterostructure, SOT originates from the bulk SHE and/or the interface Rashba–Edstein effect [9–13]. For SHE, the charge current flowing through the HM can be converted into a spin current due to the strong spin-orbit coupling (SOC). The spin current is injected from the HM to the FM layer, and a torque is applied to the FM layer, which can switch the magnetization [1, 13].

For in-plane magnetization switching driven by in-plane SOT, the critical current density for writing can be expressed as [14]

$$J_{c0} \approx \frac{2e}{\hbar}\frac{\alpha_{\mathrm{eff}}}{\theta_{\mathrm{SH}}^{\mathrm{eff}}}\left(\frac{4\pi M_{\mathrm{eff}}}{2}\right)M_s t_{\mathrm{FM}}, \tag{1}$$

where the effective spin Hall efficiency, $\theta_{\mathrm{SH}}^{\mathrm{eff}}$ represents the conversion efficiency between the charge current and the generated spin current, α_{eff} is the effective magnetic damping constant, M_{eff} is the effective magnetization, M_s is the saturation magnetization, and t_{FM} represents the ferromagnetic layer thickness. Increasing the effective spin Hall efficiency would improve the conversion efficiency of charge current to spin current in the device, achieve a low critical current threshold and increase the durability and reliability of the device [15, 16]. On the other hand, the magnetic damping constant is proportional to the critical threshold current and strongly affects the power consumption and operation speed of spintronics devices [17, 18]. Therefore, the prerequisite for achieving high performance and low power consumption in SOT-MRAM is the requirement of materials with high effective spin Hall efficiency and low effective magnetic damping constant.

Significant research efforts have been devoted to increasing the effective spin Hall efficiency in the HM/FM bilayer structures. Among various HM materials, Pt and Pt-based alloys are well-explored HMs [19, 20]. Chadova *et al* investigated the contribution of the extrinsic SHE in doped alloys based on first principles calculations. They chose Pd, Pt, and Cu as dopant acceptors and 4d (including Ag to Cd) and 5d (including Au to Hg) elements as dopant impurities and modulated the SOC strength by varying the impurity content, thus affecting the contribution of the skew scattering mechanism and the side jump mechanism [21]. Hong *et al* investigated the effective spin Hall efficiency enhancement in the Pt system by introducing Bi dopant, which was attributed by the skew scattering mechanism in the strong SOC Bi impurity [22]. Hu *et al* studied the damping-like SOT efficiency in the $Pt_xCu_{1\text{-}x}$/Co/MgO thin film and obtained the maximum damping-like SOT efficiency, excellent thermal stability, and low critical switching current density in $Pt_{0.57}Cu_{0.43}$ alloy [23]. Ramaswamy *et al* discussed the contribution of the extrinsic SHE mechanism in PtCu alloys and found that the skew scattering mechanism dominates at low Pt content; at high Pt content, the side jump mechanism contributes more [24]. Ma *et al* investigated the relationship between spin Hall efficiency and spin diffusion length for the $Pd_{1\text{-}x}Pt_x$/YIG films by varying thickness, temperature, and composition and found that the dominant mechanism is the skew scattering, and the skew scattering parameter increases with increasing spin-orbit coupling (SOC) strength [25]. Li *et al* achieved a giant spin Hall efficiency enhancement of 61.8% in $Pt_{0.77}Sn_{0.23}$ [26]. Zhu *et al* also obtained a spin Hall efficiency of up to 0.58 in $Au_{0.25}Pt_{0.75}$ [27]. Ou *et al* observed a giant spin Hall efficiency of about 0.125 in PtMn [28].

However, there are relatively limited reported studies on Pt-based alloys for various physical mechanisms of magnetic damping, as well as for the combination effects on the structure with low magnetic damping constant and high spin Hall efficiency. In the Pt-rich alloy, the scattering enhancement due to the introduction of lower atomic number Pd atoms by the extrinsic mechanism increases the spin Hall efficiency, and there is a non-monotonic variation relationship between the spin Hall efficiency and the SOC of the system [25]. Introducing a lower atomic number atom is also expected to reduce the spin pumping effect to achieve lower magnetic damping, which provides a regulatory window to achieve a high spin Hall efficiency and low damping constant [20].

In this work, we report the effective spin Hall efficiency and effective magnetic damping constant of $Pt_{1\text{-}x}Ta_x$/CoFeB thin films. The effective spin Hall efficiency of $Pt_{1\text{-}x}Ta_x$/CoFeB thin films can be enhanced by tuning the Ta concentration in the $Pt_{1\text{-}x}Ta_x$ layer, with a maximal value of 0.35 at $x = 0.15$. The interaction between the contribution of the skew scattering mechanism and the spin-orbit coupling was found to be the main mechanism for the non-monotonic behavior of the effective spin Hall efficiency as a function of x, which was confirmed by high-temperature spin-torque ferromagnetic resonance (ST-FMR) measurement. Moreover, we find that the $Pt_{1\text{-}x}Ta_x$/CoFeB films exhibit reduced effective magnetic damping and interfacial spin transparency.

2. Experimental and method

The $Pt_{1\text{-}x}Ta_x$ (5 nm)/$Co_{40}Fe_{40}B_{20}$ (5 nm) thin films were sputtered onto thermally oxidized Si substrates with (100) orientation at room temperature. The base pressure before the deposition was better than 1×10^{-7} mTorr, and the Ar gas pressure and flow during deposition were set at 2 mTorr and 20 SCCM (standard cubic centimeters per minute), respectively. The $Pt_{1-x}Ta_x$ alloy films were prepared by co-sputtering both Pt and Ta simultaneously, and their atomic composition was varied by adjusting their sputtering power. The Pt target varied between 20 to 75 W, and the Ta target was from 50 to 100 W. The sputtering power of both targets was pre-calibrated. A 2 nm Ta was deposited as a buffer layer. Single $Pt_{1-x}Ta_x$ blanket layer films were fabricated for the composition measurement by Energy-dispersive x-ray spectroscopy and the crystalline structure by x-ray diffraction (XRD). Magnetization hysteresis loops were measured using a vibrating sample magnetometer (VSM). For ST-FMR measurement, the film stacks were patterned into rectangular-shaped microstrips (length of 50 μm and width of 10 μm) using a combination of electron beam lithography (EBL) and Ar ion milling techniques. After that, Ta (5 nm)/Cu (200 nm)/Pt (3 nm) electrodes were also fabricated using EBL and liftoff following DC

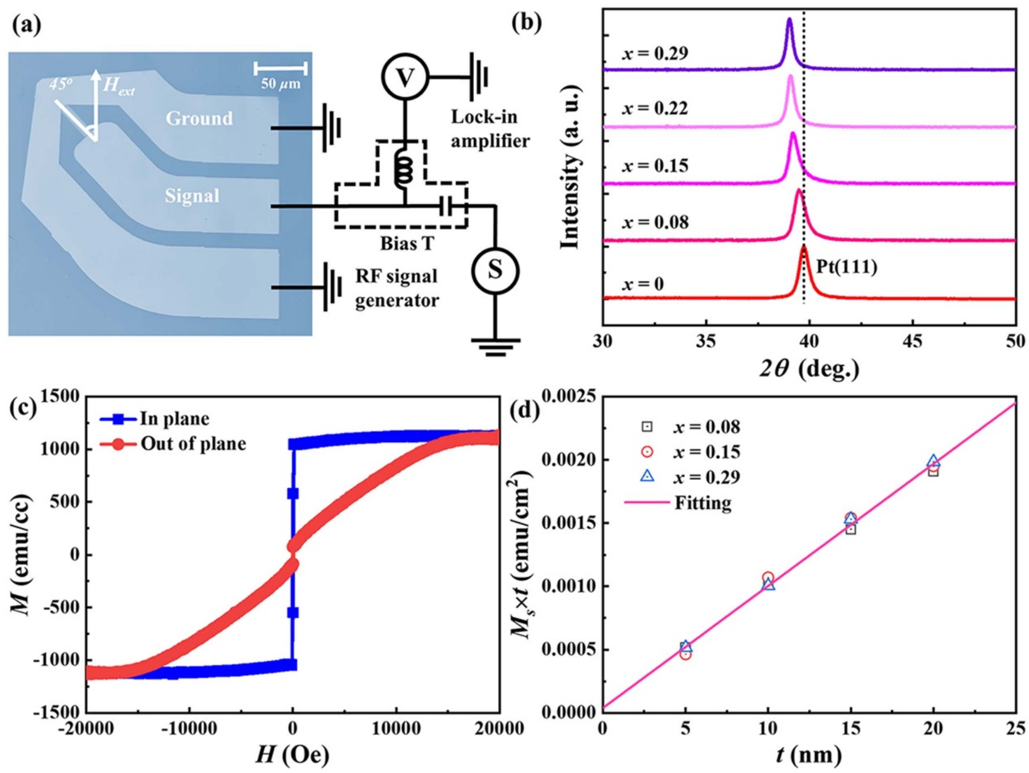

Figure 1. (a) Schematic diagrams of the device with contact pads and the experimental setup. (b) X-ray diffraction patterns for $Pt_{1\text{-}x}Ta_x$ films with different x. (c) M–H loops for $x = 0.15$ sample. (d) Saturation magnetic moment per unit area versus the CoFeB film thickness for $x = 0.08$, 0.15, 0.22 and 0.29. Symbols refer to experimental data, and solid lines are linear fits.

magnetron sputtering. A Signal Generator (Keysight N5183B) and a Network Analyzer were utilized for the ST-FMR and conventional FMR measurements were used to provide the radio frequency (RF) current, respectively. The DC voltage was measured with a Keithley 2000 multimeter for the ST-FMR measurement.

Figure 1(a) exhibits a setup schematic with an optical image of the patterned structure for the ST-FMR measurement. An RF current was applied to the microstrip along the longitudinal direction. At the same time, an external magnetic field in the sample plane was swept at 45° from 0 to 5000 Oe, with the microwave frequency fixed during each sweep. The current generates a microwave-frequency SOT on the FM layer [29]. The SOT-induced magnetization precession gives rise to an anisotropic magnetoresistance effect in the FM layer. The oscillatory resistance and RF current bring a rectified mixing voltage V_{mix} measured via a bias tee [30]. To exclude the microwave heating effect of the ST-FMR measurement, the input microwave power was varied from 13 to 20 dBm, and the DC voltage was measured, which showed in the linear regime with increasing power (see supplementary materials for details). The measured VS/VA was independent of the applied RF power, suggesting that the microwave heating effect is relatively negligible. All measurements were performed at the RF power of 18 dBm. The ST-FMR spectra were measured for microwave frequencies from 8 to 16 GHz for all samples. The temperature dependence of the magnetic damping constant and spin Hall efficiency of the films were characterized by utilizing a homemade high-temperature ST-FMR with a temperature range of 300–450 K. The temperature calibration was performed by applying an infrared thermometer. For high-temperature ST-FMR measurements, the non-magnetic heating element was positioned directly below the sample stage pre-heating the sample for 20 min before and throughout the measurement [31].

3. Results and discussion

The XRD patterns of the single $Pt_{1\text{-}x}Ta_x$ layer film are shown in figure 1(b). When no Ta is incorporated, there is a strong diffraction peak on the XRD pattern at $2\theta = 39.8°$, indicating a highly (111)-oriented texture in the Pt film. With Ta content increasing, no other phase appears. As the Ta content increases, the (111) peak moves to the left to a lower angle, indicating that the Ta atoms enter the Pt lattice, which leads to lattice expansion (increase in the crystal plane distance d). Since the diameter of Ta atoms is larger than that of Pt, the possibility of Ta atom occupation substitution is higher than vacancy doping [22, 31]. Figure 1(c) shows the hysteresis loops of $Pt_{0.85}Ta_{0.15}$/CoFeB films along the in-plane and out-of-plane different directions, which exhibits in-plane magnetic anisotropy. The value of saturation magnetization measured by VSM is 1135 emu cc^{-1}, which is consistent with the previous reports [17, 32]. Figure 1(d) reveals the saturation magnetic moment per unit area of $Pt_{1-x}Ta_x$/CoFeB films versus

CoFeB layer thickness for Ta content of 0.08, 0.15, and 0.29, respectively. By linear fitting, the saturation magnetization M_S and the thickness of the magnetic dead layer can be obtained from the slope and the intersection with the horizontal axis, respectively [33]. From the results of the fit, it can be seen that the slope does not change almost with the composition of $Pt_{1-x}Ta_x$, and the thickness of the magnetic dead layer is close to zero, indicating that the magnetic variation due to the magnetic proximity effect and the effect of the magnetic dead layer can be neglected [27].

Figure 2(a) shows the ST-FMR spectra V_{mix} for the $Pt_{1-x}Ta_x$ /CoFeB devices with $x = 0.2$ measured at a frequency range of 8–16 GHz. The resonance peak changes its sign by reversing the direction of the external magnetic field $\boldsymbol{H}$, suggesting that the damping-like torque is dominant compared to the Oersted field, which is consistent with the prediction of the spin-torque driven FMR [34]. The effective magnetization $4\pi M_{eff}$ can be obtained by fitting the resonance frequency f to the resonance field H_{res} using Kittel's equation due to the negligibly small in-plane magnetic anisotropy [29], as shown in the inset in figure 2(a), yielding a value of 1.426 T for $4\pi M_{eff}$, which is consistent with the value of M_s determined by the VSM considering the contribution of the out-of-plane anisotropic field to the effective magnetization.

Figures 2(b) and (c) show the fitting of a ST-FMR spectrum measured at a frequency of 14 GHz for the $Pt_{1-x}Ta_x$/CoFeB devices with $x = 0$ and $x = 0.15$. The signal can be decomposed into the symmetric and antisymmetric Lorentzian components, which are represented by the pink and blue curves, respectively. The measured mixing DC voltage V_{mix} is expressed as [29, 35]

$$V_{mix} = V_S \frac{(\Delta H)^2}{(\Delta H)^2 + (\mu_0 H - \mu_0 H_{res})^2} + V_A \frac{\Delta H (\mu_0 H - \mu_0 H_{res})}{(\Delta H)^2 + (\mu_0 H - \mu_0 H_{res})^2} \quad (2)$$

where ΔH, H_{res}, V_S, and V_A are the resonance linewidth, the resonance magnetic field, the amplitudes of the symmetric and anti-symmetric component of the mixing voltage, respectively [36].

$$V_S = \frac{\Delta R I_{rf}}{2} \mu_0 h_z \sin 2\theta \frac{\mu_0 H_{res} + \mu_0 M_S}{\Delta H (2\mu_0 H_{res} + \mu_0 M_S)} \frac{1}{\sqrt{1 + \frac{\mu_0 M_S}{\mu_0 H_{res}}}} \quad (3)$$

$$V_A = \frac{\Delta R I_{rf}}{2} \mu_0 h_y \sin 2\theta \cos\theta \frac{\mu_0 H_{res} + \mu_0 M_S}{\Delta H (2\mu_0 H_{res} + \mu_0 M_S)}, \quad (4)$$

where ΔR is the resistance change of the bilayer due to the anisotropic magnetoresistance, I_{rf} is the amplitude of the RF current, and $\mu_0 M_S$ is the saturation magnetization of the CoFeB layer. Here, the out-of-plane effective field h_z is proportional to the damping-like torque, which is due to pure spin current generated by the SHE, and h_y is in-plane effective field dominated by the Oersted filed. It is clear that the symmetric component voltage V_S dominates more in the spectrum for $x = 0.15$ compared to $x = 0$, representing a greater contribution of the damping-like torque in the system.

The dependence of the ratio V_S/V_A between the symmetric and asymmetric components on the Ta content is given in figure 2(d). From the line shape of the ST-FMR spectra, the effective spin Hall efficiency θ_{SH}^{eff} can be extracted for a qualitative dependence according to the ST-FMR theory [29, 37], $\theta_{SH}^{eff} = \frac{eJ_S}{J_C} = \frac{V_s}{V_A} \frac{e\mu_0 M_S td}{\hbar} \left(1 + \frac{4\pi M_{eff}}{H_{res}}\right)^{1/2}$. The value of the effective spin Hall efficiency obtained using the linear method is biased due to the use of a Ta buffer layer that partially cancels the Oster field generated by the current in $Pt_{1-x}Ta_x$ [16]. Nevertheless, V_S/V_A can still reflect the magnitude of the effective spin Hall efficiency of the system, and a larger V_S/V_A means a larger effective spin Hall efficiency. As shown in figure 2(d), θ_{SH}^{eff} increases and then decreases with increasing Ta content and reaches a maximum value of $\theta_{SH}^{eff} = 0.35$ at $x = 0.15$. The peak is similar to that at Pt-rich concentrations in PdPt alloys [25, 38, 39]. We suggest that it comes from the contribution of the extrinsic SHE mechanism, such as the skew scattering mechanism and the side jump mechanism. The observation can be ascribed to a competition between the enhanced electron scattering that increases as a function of increasing Ta content and the strength of SOC, which decreases as Ta content increases. For lower Ta content, the enhancement of electron scattering is larger than the decrease in the SOC, which results in the enhancement of effective spin Hall efficiency. While for higher Ta content, the reduction of the SOC strength is larger than the increase in scattering, which leads to the reduction in effective spin Hall efficiency.

It is noted that since the effective spin Hall efficiency sign of Pt is opposite to that of Ta, there may be a compensation of the SHE or a contribution of the spin accumulation caused by the sign reversal to the effective spin Hall efficiency. Han *et al* observed that the spin accumulation caused by the SHE at the Ta-Pt grain boundary was in $Ta_{1-x}Pt_x$ [40]. Their calculations obtained the interfacial spin-dependent electrochemical potential (μ_S^*) with a similar trend to that of the effective spin Hall efficiency at low concentration levels in this study. In comparison, spin accumulation at the W/Pt interface was also observed in YIG/Pt/W and Py/W/Pt by Luan *et al* [41] and Karube *et al* [42], respectively. Luan *et al* found enhanced spin Hall magnetoresistivity originating from the spin accumulation at the interface [41]. Additional spin-orbit fields with the variation of the W layer thickness were also found by Karube *et al* [42]. In this work, only one strong (111) peak was observed in the diffraction pattern of XRD, and no peak of Ta was observed. And effective spin accumulation is considered to require the presence of clear and sharp grain boundaries between the grains of Ta and Pt with grain size in the nanometer scale, comparable to the spin diffusion length [40]. The synergistic effect of magnetically ordered layers together in Pt induced by the magnetic nearest neighbor effect is also required. Therefore, it is believed that the additional contribution of the effective spin Hall efficiency due to spin accumulation in this experiment can be excluded.

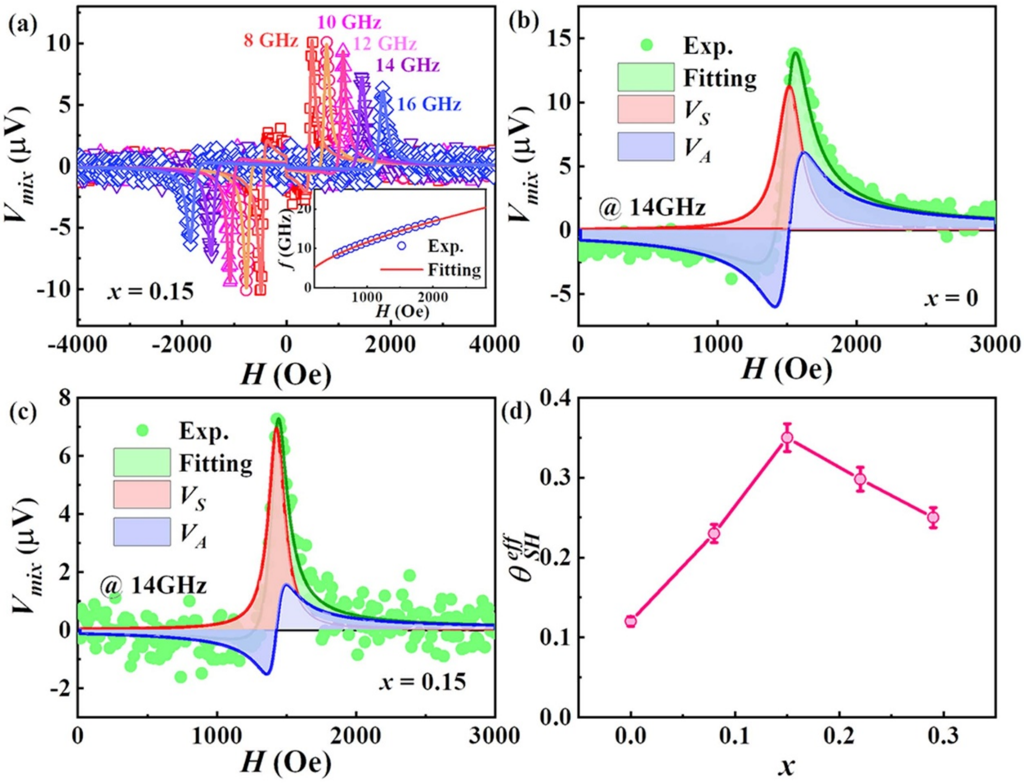

Figure 2. (a) The ST-FMR spectra for different RF current frequencies from 8 to 16 GHz for the $x = 0.15$ devices, the inset shows frequency as a function of the resonant field used in the Kittel formula fitting. $V_{\rm mix}$ along with the fitted (green), symmetric ($V_{\rm S}$, red), and antisymmetric ($V_{\rm A}$, blue) Lorentzian functions used for the fitting measured at 14 GHz for $Pt_{1-x}Ta_x$/CoFeB films with (b) $x = 0$ and (c) $x = 0.15$. (d) Dependence of the $\theta_{\rm SH}^{\rm eff}$ on x.

As for the compensation of effective spin Hall efficiency due to the opposite sign, Uchida *et al* and Qu *et al* observed a linear variation of effective spin Hall efficiency with composition in PtW and AuTa with the number of valence electrons [43, 44], respectively. Miao *et al* also observed in the TaPt alloy system that the effective spin Hall efficiency increases with increasing Pt content from a negative sign in the Ta-rich region to a positive sign in the Pt-rich region, which is different from the non-monotonic variation here [45]. Similar enhancements to this work were observed by Laczkowski *et al* in AuW and AuTa alloys with low doping content of opposite effective spin Hall efficiency sign, where the main mechanism in AuW and AuTa are the intrinsic mechanism and Ta impurity-induced side jump mechanism, respectively [46]. In this work, since Ta is in the lightly doped range and the SHE of Pt while much stronger than α-Ta, the offsetting effect is weak within the Pt-rich content and mainly exhibits an extrinsic SHE due to Ta impurities.

To further exclude the effects of other extrinsic effects and clarify the origin of the symmetric component $V_{\rm S}$ and the asymmetric component $V_{\rm A}$ of the ST-FMR signal, the field-angle θ dependence of $V_{\rm S}$ and $V_{\rm A}$ extracted from the $V_{\rm mix}$ signals measured at $f = 14$ GHz for $Pt_{1-x}Ta_x$/CoFeB bilayer with $x = 0$ and $x = 0.15$ are shown in figure 3. As shown in figures 3(a) and (b), the $V_{\rm S}$ as a function of θ is fitted well by a function proportion to $\sin2\theta\,\cos\theta$ with $x = 0$ and $x = 0.15$, indicating an angular dependence of the out-of-plane effective field h_z proportional to $\cos\theta$. This angular dependence is the same as the angular dependence of the spin torque [36]. And according to the spin torque mechanism, its angular dependence is caused by the spin flow being absorbed by the ferromagnetic layer due to the SHE in the HM layer, which generates a damping-like moment. Therefore, it can be confirmed that V_S in this chapter should come mainly from the contribution of the SHE. As a comparison, figures 3(c) and (d) show the variation of $V_{\rm A}$ with the angle for $x = 0$ and $x = 0.15$, fitted by the $\sin2\theta\cos\theta$ function [36]. The results can be well described, showing that the in-plane effective field h_y has no angular dependence. According to previous reports, it is shown that the Oster field mainly dominates V_A [35]. Since both $V_{\rm S}$ and $V_{\rm A}$ can be well fitted to $\sin2\theta\cos\theta$, while the spin-Seebeck effect induces $V_{\rm S}$ proportional to $\sin\theta$, the spin-orientation effect also leads to deviations in the fit, indicating that the spin-Seebeck effect in this experiment and the spin-orientation effect may cause additional contributions can both be neglected [47–49].

The effective damping constant ($\alpha_{\rm eff}$) for $Pt_{1-x}Ta_x$/CoFeB films with $x = 0$ and $x = 0.15$ is evaluated by fitting the ΔH versus f data using the equation $\Delta H = \Delta H_{\rm inh} + 2\pi f\alpha_{\rm eff}/\gamma$ [29] as shown in figure 4(a), where $\Delta H_{\rm inh}$ is the frequency independent linewidth contribution from inhomogeneity in the magnetic film. From the fitting, the effective damping constant was found to be 6.6×10^{-3}, which is lower than the value of $x = 0$ ($\sim 11.7 \times 10^{-3}$). The inhomogeneous linewidth is found to be 15.2 Oe, which indicates a smooth interface and

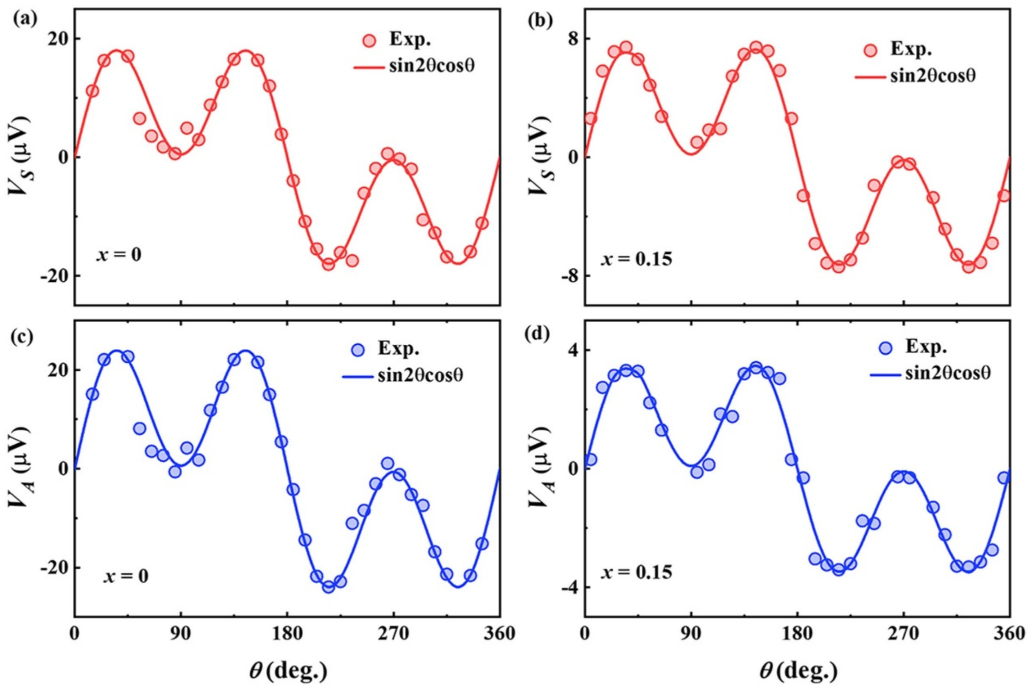

Figure 3. Magnet field angle θ dependence of the V_S of the ST-FMR spectra for $Pt_{1-x}Ta_x$/CoFeB films with (a) $x = 0$ and (b) $x = 0.15$. Magnet field angle θ dependence of the V_A of the ST-FMR spectra for $Pt_{1-x}Ta_x$ /CoFeB films with (c) $x = 0$ and (d) $x = 0.15$.

a high quality of the $Pt_{1-x}Ta_x$/CoFeB films [50]. Furthermore, the ΔH vs f response in figure 4(a) shows a linear behavior over the entire frequency range, suggesting a negligible contribution from the non-linear two-magnon scattering mechanisms in the $Pt_{1-x}Ta_x$/CoFeB films [51]. The dependence of the effective damping constant on x is given in figure 4(b). As Ta content increases from 0 to 0.29, the value of α_{eff} decreases from 11.7×10^{-3} to 5.9×10^{-3} ($\Delta\alpha/\alpha_0 \sim -49.6\%$ for $x = 0.29$). However, the effective damping constants in the $Pt_{1-x}Ta_x$/CoFeB are larger than the intrinsic damping in amorphous CoFeB thin film ($\sim 4.0 \times 10^{-3}$) [32]. Therefore, it is suggested that there is an extrinsic contribution of the magnetic damping mechanism in the $Pt_{1-x}Ta_x$/CoFeB films.

The contribution of the extrinsic magnetic damping mechanism may come from various interfacial effects, such as the magnetic proximity effect, the effect of the magnetic dead layer, and the spin pumping effect [52–54]. According to the discussion above, the thickness of the magnetic dead layer obtained for the samples with different CoFeB thicknesses is minimal. It does not change significantly with increasing Ta, and its effect on the magnetic damping constant can be excluded. Secondly, since the M_s of the ferromagnetic layer is smaller than the value of the bulk and remains constant with the change of Ta content, the contribution of the magnetic proximity effect can be considered negligible. Thus, the contribution of the extrinsic magnetic damping can be attributed to the angular momentum loss due to the spin-pumping effect [55]. And this additional damping contribution originates from the effect of spin-orbit coupling. The spin-orbit coupling effect is proportional to the fourth power of the atomic number, which is 73 for Ta, which is smaller than 79 for Pt. Therefore, the decrease in the effective magnetic damping constant indicates that the spin-orbit coupling strength at the $Pt_{1-x}Ta_x$/CoFeB interface decreases with increasing Ta content. Using equation (1), the critical switching current density J_{c0} is calculated using the data in figures 2(d) and 4(b), and the normalized result is plotted in figure 4(c). It can be seen that the calculated J_{c0} at $x = 0.15$ is much smaller than that at $x = 0$ and is only 16% of that at $x = 0$ due to a combination of lower α_{eff} and larger $\theta_{\mathrm{SH}}^{\mathrm{eff}}$, which shows excellent potential applications as spin Hall material for achieving low-power consumption SOT devices [14, 56].

The dependence of the enhanced damping $\Delta\alpha$ on the thickness of the non-magnetic layer is given in figure 4(d). As the thickness increases, $\Delta\alpha$ increases with different Ta contents in the lower thickness range, while α tends to saturation values at higher thicknesses. It can be seen that the $x = 0$ sample reached saturation first for the non-magnetic layer thickness, $x = 0.15$ came saturation values at larger non-magnetic layer thicknesses, and their saturation value of damping is lower than that of the Pt sample. Also, since the contribution of the magnetic proximity effect to the magnetic damping has a strong quasi-linear relationship with the nonmagnetic layer thickness, this nonlinear behavior between the increased magnetic damping and thickness can exclude the mechanism originating from the contribution of the extrinsic damping caused by the magnetic proximity effect. A spin-pumping model was used to describe the variation of damping with the non-magnetic layer [55], from which the spin mixing conductance $G^{\uparrow\downarrow}$ and spin diffusion length λ_{sd} are found to be 37.6×10^{14} cm^{-2} (10.2×10^{14} cm^{-2}) and 2.8 nm (4.1 nm), respectively. λ_{sd} obtained for $x = 0$ is slightly larger than the value reported by Nakayama *et al* (2.4 nm) [57], but smaller than the value

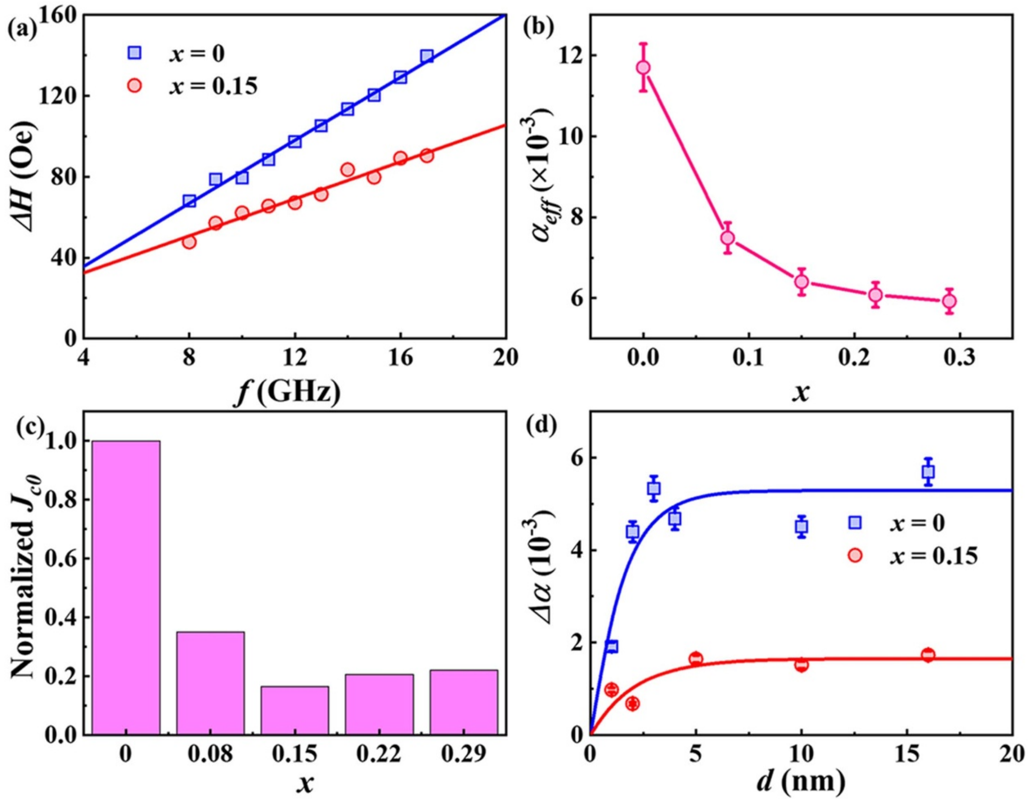

Figure 4. (a) The linewidth as a function of frequency for $Pt_{1-x}Ta_x$/CoFeB films with $x = 0$ and $x = 0.15$. Dependence of the effective magnetic damping constant (b) and the normalized switching current density (c) on x. (d) Enhanced damping $\Delta\alpha$ as a function of non-magnetic layer thickness for $Pt_{1-x}Ta_x$/CoFeB films with $x = 0$ and $x = 0.15$.

reported by Liu *et al* (3.0 nm) [29], which is consistent with the previously reported values.

According to the Elliott–Yafet model, the spin-flip scattering rate contains two components [58, 59]: the first originates from the spin-orbit coupling near the impurity; the second arises from the interaction between the photon and the spin-orbit coupling. The first term is related to the angular momentum scattering rate due to impurities and is independent of temperature. The spin diffusion length is inversely proportional to the scattering cross section for lightly doped alloys due to spin-orbit coupling [60]. For the second term, the spin-flip scattering rate is proportional to the square of the spin-orbit coupling parameter [61]. These two contributions lead to an increase in the spin-flip scattering rate with increasing spin-orbit coupling strength. Thus, the spin-orbit coupling is weakened due to Ta content increasing, and the spin diffusion length increases compared to pure Pt.

Based on the spin-diffusion model, the interfaces spin transparency was estimated [62]. Using the extracted values of $G^{\uparrow\downarrow}$ versus λ_{sd}, the interface spin transparency for the $x = 0$ and $x = 0.15$ samples were calculated to be 58.8% and 41.4%, respectively. The value of the interface spin transparency at $x = 0$ is slightly smaller than the 65% reported by Zhang *et al* [62] and 63% reported by Huang *et al* [16] for the Pt/CoFeB interface, which may be originated from the difference in the obtained spin-diffusion lengths. While for the $x = 0.15$, the decrease in spin transparency mainly comes from the reduction in spin mixing conductance with the increase in spin diffusion length. The value of spin transparency for this interface is similar to 50% of that for the β-Ta/CoFeB interface [63], but still in the range for the Pt/Co interface (30%–60%) [62, 64] and is larger than the value for the *Pt/Py* interface (25%) [62].

Figure 5(a) shows the dependence of $Pt_{0.85}Ta_{0.15}$/CoFeB microwave frequency versus resonance field. By fitting the Kittel equation, the normalized effective magnetization $M_{eff}(T)/M_{eff}(0)$ with temperature can be obtained as in the inset of figure 5(a). The $M_{eff}(T)/M_{eff}(0)$ decreases with increasing temperature. The curve can be fitted using the empirical equation $M_s(T) = M_s(0)[(1-(T/T_C)^2]^{1/2}$, and the Curie temperature can be determined [65], from which the T_C is obtained to be about 980.5 K [66]. It is consistent with the reported Curie temperature of CoFeB films. The variation of the linewidth with frequency at different temperatures is shown in figure 5(b). The linewidths of the Pt/CoFeB samples are higher than those of $Pt_{0.85}Ta_{0.15}$/CoFeB throughout the temperature range 320–460 K. In addition, no significant nonlinear deviation of the resonance linewidths with frequency variation is observed, so the contribution of the two-magnon scattering mechanism in this temperature range can be excluded [51].

The dependence of the effective magnetic damping constant α_{eff} with temperature is given in figure 5(c). In the temperature range of 320–460 K, a for $x = 0$ decreases by 16.9%

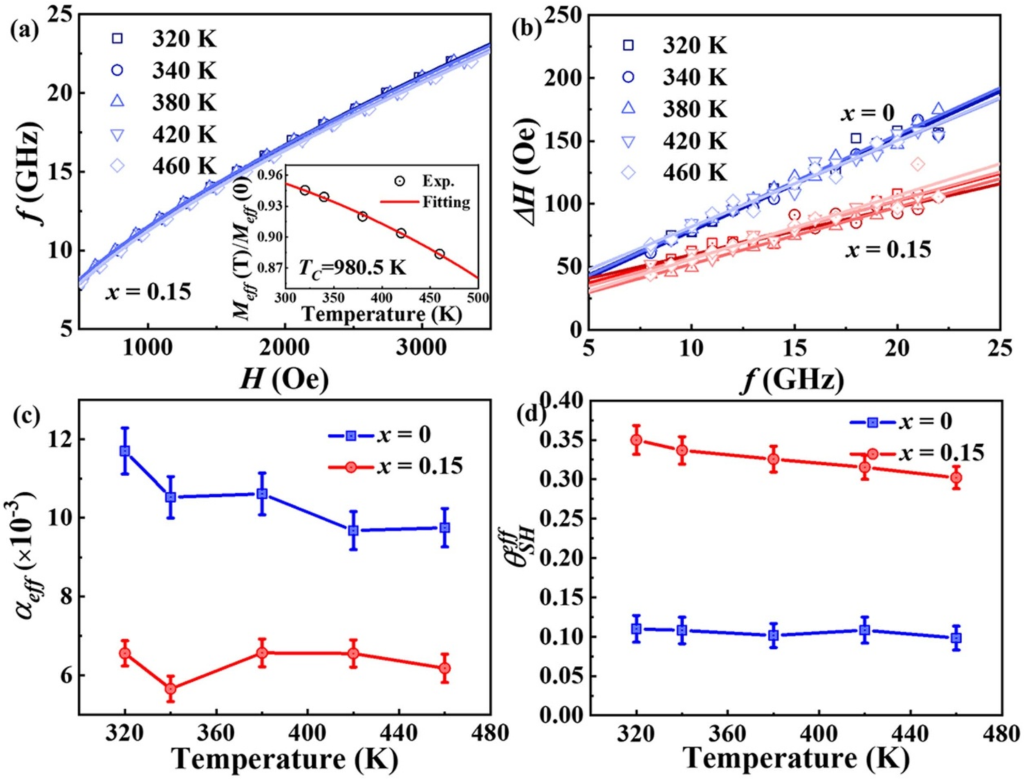

Figure 5. (a) The f vs H_{res} plot for $\mathrm{Pt_{0.85}Ta_{0.15}}$/CoFeB film at different temperatures, and the inset shows the normalized effective magnetization as a function of temperature. (b) Variation of ΔH with f for $\mathrm{Pt_{1\text{-}x}Ta_x}$/CoFeB films with $x = 0$ and $x = 0.15$ at different temperatures. The (c) α_{eff} and (d) $\theta_{\mathrm{SH}}^{\mathrm{eff}}$ as a function of temperature for $\mathrm{Pt_{1\text{-}x}Ta_x}$/CoFeB films with $x = 0$ and $x = 0.15$.

with increasing temperature, while a for $x = 0.15$ does not change significantly with only a 5.6% drop, demonstrating good thermal stability of the magnetic damping constant for $x = 0.15$. It indicates a different magnetic damping mechanism for both. According to the analysis above, the main sources of the magnetic damping constant here are the intrinsic Gilbert damping and the spin-pumping effect. In the case of Gilbert damping, according to the torque-dependent model [67], the intraband scattering mode's contribution can be neglected because the amorphous CoFeB film's intraband scattering mode vanishes. Only the effect of interband scattering needs to be considered [68]. As the temperature increases, the interband scattering effect enhances, the spin relaxation contribution increases, and the intrinsic Gilbert damping rises. In contrast, in the temperature range of 320–460 K, the spin-orbit coupling effect weakens and the spin-pumping effect diminishes as the temperature increases. For the $x = 0$ sample, the damping is dominated by the spin-pumping effect, so the effective magnetic damping constant decreases when the temperature increases. For $x = 0.15$, the Ta alloyed Pt weakens the interfacial spin-orbit coupling, the damping contributed by the spin-pumping effect weakens, and the intrinsic Gilbert damping becomes significant. Two damping mechanisms with opposite temperature dependence act together as the temperature increases, so the total effective magnetic damping constant does not vary significantly [68].

The $\theta_{\mathrm{SH}}^{\mathrm{eff}}$ as a function of temperature for $\mathrm{Pt_{1\text{-}x}Ta_x}$/CoFeB films with $x = 0$ and $x = 0.15$ are presented in figure 5(d). There is a 9.1% decrease in $\theta_{\mathrm{SH}}^{\mathrm{eff}}$ with increasing temperature for $x = 0$ over the whole temperature range, while $\theta_{\mathrm{SH}}^{\mathrm{eff}}$ for $x = 0.15$ is more temperature sensitive and decrease by 14.5% with the increasing temperature. Since the skew scattering mechanism is considered independent of the change in temperature due to its independent resistivity, the intrinsic and side jump mechanisms have a temperature dependence due to their resistivity dependence [31]. The temperature dependence of Pt was observed in the temperature range 13–300 K by Wang *et al*, who concluded that the intrinsic mechanism is not its dominant mechanism [19]. Isasa *et al* observed a weak change in the effective spin Hall efficiency from 10 K to 300 K in Pt. Although the amount of change is small, this increase is thought to originate mainly from the intrinsic mechanism [69]. Phu *et al* observed a slight increase of about 2% in the effective spin Hall efficiency of Pt in the temperature range of 300–410 K and concluded that the skew scattering mechanism plays a non-negligible role [66]. Chen *et al* observed a 3% increase in the effective spin Hall efficiency of β-W with increasing temperature at 10–300 K [70]. Niimi *et al* found a temperature-independent increase in the effective spin Hall efficiency for Ir content in the range of 1%–12% in CuIr alloys [71]. Therefore, the temperature variation relation of $\theta_{\mathrm{SH}}^{\mathrm{eff}}$ for $x = 0.15$ can be used as proof of the predominant side-jump scattering contribution with this region. Combined the magnetic damping constant and spin Hall efficiency dependence on temperature, for $x = 0.15$, a lower value and less temperature sensitivity of $\alpha_{\mathrm{eff}}/\theta_{\mathrm{SH}}^{\mathrm{eff}}$ can be achieved, which could reduce the switching current density for magnetization reversal.

4. Conclusion

In summary, the effective spin Hall efficiency and effective magnetic damping constant of $Pt_{1-x}Ta_x$/CoFeB films are investigated. With the Ta content increasing, the effective spin Hall efficiency increases and then decreases, and an enhancement by a factor of 190% is reached at $x = 0.15$. This non-monotonic variation can be explained by the interaction between the contribution of the skew scattering mechanism, which increases with increasing Ta content, and the spin-orbit coupling, which decreases with increasing Ta content. The effective magnetic damping constant decreases with increasing Ta content, indicating that the spin-orbit coupling of the system is weakened. According to the EY spin relaxation mechanism, the doping of Ta weakens the spin-orbit coupling and increases the spin diffusion length. The interfacial spin transparency is reduced due to the decreased spin mixing conductance and the increased spin diffusion length. In addition, the high-temperature ST-FMR measurement also demonstrates that the doping of Ta leads to a weakening of the spin-orbit coupling, and the contribution of the skew scattering mechanism in the extrinsic SHE is dominant. Our findings provide an efficient spin Hall material system that simultaneously combines a significant SHE and a low damping factor to effectively reduce the critical switching current for developing low-power consumption spintronic devices.

Data availability statement

All data that support the findings of this study are included within the article (and any supplementary files).

Acknowledgments

This work was supported by a RIE2020 AME IAF-ICP Grant (No. I1801E0030). This work was also supported by an EDB-IPP (RCA-17/284) Grant. This work was also supported by a jit-b-202361 Grant. Z Xu gratefully acknowledges financial support from the China Scholarship Council. We thank W L Gan and G D H Wong for the discussion that led to this work.

ORCID iDs

Zhan Xu https://orcid.org/0000-0003-1224-9789
Er Liu https://orcid.org/0000-0001-9534-7469
Feng Xu https://orcid.org/0000-0001-5802-7925
Leixiang Bian https://orcid.org/0000-0002-8248-586X
Wen Siang Lew https://orcid.org/0000-0002-5161-741X

References

[1] Song C, Zhang R, Liao L, Zhou Y, Zhou X, Chen R, You Y, Chen X and Pan F 2020 Spin-orbit torques: materials, mechanisms, performances, and potential applications *Prog. Mater. Sci.* **116** 100761
[2] Avci C O, Quindeau A, Pai C-F, Mann M, Caretta L, Tang A S, Onbasli M C, Ross C A and Beach G S D 2017 Current-induced switching in a magnetic insulator *Nat. Mater.* **16** 309–14
[3] Ryu J, Lee S, Lee K and Park B 2020 Current-induced spin–orbit torques for spintronic applications *Adv. Mater.* **32** 1907148
[4] Li Y, Edmonds K W, Liu X, Zheng H and Wang K 2019 Manipulation of magnetization by spin-orbit torque *Adv. Quantum Technol.* **2** 1800052
[5] Ang C C I, Gan W, Wong G D H and Lew W S 2020 Electrical control of skyrmion density via skyrmion-stripe transformation *Phys. Rev. Appl.* **14** 054048
[6] Onoda M, Murakami S and Nagaosa N 2004 Hall effect of light *Phys. Rev. Lett.* **93** 083901
[7] Zhen W, Wang X-L, Ding J and Wang H-T 2023 Controlling the symmetry of the photonic spin Hall effect by an optical vortex pair *Phys. Rev. A* **108** 023514
[8] Liu S, Chen S, Wen S and Luo H 2022 Photonic spin Hall effect: fundamentals and emergent applications *Opto-Electron. Sci.* **1** 220007
[9] Liu L, Lee O J, Gudmundsen T J, Ralph D C and Buhrman R A 2012 Current-induced switching of perpendicularly magnetized magnetic layers using spin torque from the spin Hall effect *Phys. Rev. Lett.* **109** 096602
[10] Yu G *et al* 2014 Switching of perpendicular magnetization by spin-orbit torques in the absence of external magnetic fields *Nat. Nanotechnol.* **9** 548–54
[11] Luo F, Wong Q Y, Li S, Tan F, Lim G J, Wang X and Lew W S 2019 Dependence of spin-orbit torque effective fields on magnetization uniformity in Ta/Co/Pt structure *Sci. Rep.* **9** 10776
[12] Poh H Y, Ang C C I, Jin T L, Tan F N, Lim G J, Wu S, Poh F and Lew W S 2022 Continuous film spin-orbit torque characterization via four probe measurement *Appl. Phys. Lett.* **121** 012405
[13] Hwee Wong G D *et al* 2021 Strain-mediated spin-orbit torque enhancement in Pt/Co on flexible substrate *ACS Nano* **15** 8319–27
[14] Lee D, Kim J, Park H, Lee K-J, Ju B-K, Koo H C, Min B-C and Lee O 2018 Spin-orbit torque and magnetic damping in tailored ferromagnetic bilayers *Phys. Rev. Appl.* **10** 024029
[15] Miron I M, Garello K, Gaudin G, Zermatten P-J, Costache M V, Auffret S, Bandiera S, Rodmacq B, Schuhl A and Gambardella P 2011 Perpendicular switching of a single ferromagnetic layer induced by in-plane current injection *Nature* **476** 189–93
[16] Huang L, He S, Yap Q J and Lim S T 2018 Engineering magnetic heterostructures to obtain large spin Hall efficiency for spin-orbit torque devices *Appl. Phys. Lett.* **113** 022402
[17] Ikeda S, Miura K, Yamamoto H, Mizunuma K, Gan H D, Endo M, Kanai S, Hayakawa J, Matsukura F and Ohno H 2010 A perpendicular-anisotropy CoFeB–MgO magnetic tunnel junction *Nat. Mater.* **9** 721–4
[18] Haidar M, Awad A A, Dvornik M, Khymyn R, Houshang A and Åkerman J 2019 A single layer spin-orbit torque nano-oscillator *Nat. Commun.* **10** 2362
[19] Wang Y, Deorani P, Qiu X, Kwon J H and Yang H 2014 Determination of intrinsic spin Hall angle in Pt *Appl. Phys. Lett.* **105** 152412
[20] Nguyen M-H, Zhao M, Ralph D C and Buhrman R A 2016 Enhanced spin Hall torque efficiency in $Pt_{100-x}Al_x$ and

$Pt_{100-x}Hf_x$ alloys arising from the intrinsic spin Hall effect *Appl. Phys. Lett.* **108** 242407
[21] Chadova K, Wimmer S, Ebert H and Ködderitzsch D 2015 Tailoring of the extrinsic spin Hall effect in disordered metal alloys *Phys. Rev.* B **92** 235142
[22] Hong C, Jin L, Zhang H, Li M, Rao Y, Ma B, Li J, Zhong Z and Yang Q 2018 Giant inverse spin hall effect in Bi doped PtBi alloy *Adv. Electron. Mater.* **4** 1700632
[23] Hu C and Pai C 2020 Benchmarking of spin–orbit torque switching efficiency in Pt alloys *Adv. Quantum Technol.* **3** 2000024
[24] Ramaswamy R, Wang Y, Elyasi M, Motapothula M, Venkatesan T, Qiu X and Yang H 2017 Experimental study of extrinsic spin Hall effect in CuPt alloy *Phys. Rev. Appl.* **8** 024034
[25] Ma L, Lang L, Kim J, Yuan Z, Wu R, Zhou S and Qiu X 2018 Spin diffusion length and spin Hall angle in Pd1-xPtx/YIG heterostructures: examination of spin relaxation mechanism *Phys. Rev.* B **98** 224424
[26] Li M, Jin L, Rao Y H, Zhong Z, Tang X, Liu B, Meng H, Yang Q, Lin Y and Zhang H 2020 Large spin Hall angle in nonmagnetic PtSn alloy films at room temperature *J. Magn. Magn. Mater.* **507** 166860
[27] Zhu L, Ralph D C and Buhrman R A 2018 Highly efficient spin-current generation by the spin hall effect in $Au_{1-x}Pt_x$ *Phys. Rev. Appl.* **10** 031001
[28] Ou Y, Shi S, Ralph D C and Buhrman R A 2016 Strong spin Hall effect in the antiferromagnet PtMn *Phys. Rev.* B **93** 220405
[29] Liu L, Moriyama T, Ralph D C and Buhrman R A 2011 Spin-torque ferromagnetic resonance induced by the Spin Hall effect *Phys. Rev. Lett.* **106** 036601
[30] Xu Z, Wong G D H, Tang J, Liu E, Gan W, Xu F and Lew W S 2021 Large spin Hall angle enhanced by nitrogen incorporation in Pt films *Appl. Phys. Lett.* **118** 062406
[31] Wong G D H, Law W C, Tan F N, Gan W L, Ang C C I, Xu Z, Seet C S and Lew W S 2020 Thermal behavior of spin-current generation in Pt_xCu_{1-x} devices characterized through spin-torque ferromagnetic resonance *Sci. Rep.* **10** 9631
[32] Conca A, Greser J, Sebastian T, Klingler S, Obry B, Leven B and Hillebrands B 2013 Low spin-wave damping in amorphous $Co_{40}Fe_{40}B_{20}$ thin films *J. Appl. Phys.* **113** 213909
[33] Liu T, Zhang Y, Cai J W and Pan H Y 2015 Thermally robust Mo/CoFeB/MgO trilayers with strong perpendicular magnetic anisotropy *Sci. Rep.* **4** 5895
[34] An H, Ohno T, Kanno Y, Kageyama Y, Monnai Y, Maki H, Shi J and Ando K 2018 Current-induced magnetization switching using an electrically insulating spin-torque generator *Sci. Adv.* **4** eaar2250
[35] Musha A, Kanno Y and Ando K 2019 Extrinsic-intrinsic crossover of the spin Hall effect induced by alloying *Phys. Rev. Mater.* **3** 054411
[36] An H, Kanno Y, Asami A and Ando K 2018 Giant spin-torque generation by heavily oxidized Pt *Phys. Rev.* B **98** 014401
[37] Zhou J *et al* 2019 Large spin-orbit torque efficiency enhanced by magnetic structure of collinear antiferromagnet IrMn *Sci. Adv.* **5** eaau6696
[38] Zhou X, Tang M, Fan X L, Qiu X P and Zhou S M 2016 Disentanglement of bulk and interfacial spin Hall effect in ferromagnet/normal metal interface *Phys. Rev.* B **94** 144427
[39] Zhu L, Sobotkiewich K, Ma X, Li X, Ralph D C and Buhrman R A 2019 Strong damping-like spin-orbit torque and tunable Dzyaloshinskii–Moriya interaction generated by low-resistivity $Pd_{1-x}Pt_x$ alloys *Adv. Funct. Mater.* **29** 1805822
[40] Han J H, Shi G Y, Zhou X J, Yang Q H, Rao Y H, Li G, Zhang H W, Pan F and Song C 2016 Vertical spin Hall magnetoresistance in $Ta_{1-x}Pt_x$/YIG bilayers *Phys. Rev.* B **94** 134406
[41] Luan Z Z, Zhou L F, Wang P, Zhang S, Du J, Xiao J, Liu R H and Wu D 2019 Enhanced spin accumulation in metallic bilayers with opposite spin Hall angles *Phys. Rev.* B **99** 174406
[42] Karube S, Tezuka N, Kohda M and Nitta J 2020 Anomalous spin-orbit field via the Rashba-Edelstein effect at the W/Pt interface *Phys. Rev. Appl.* **13** 024009
[43] Uchida K-I, Sasaki M, Sakuraba Y, Iguchi R, Daimon S, Saitoh E and Goto M 2018 Combinatorial investigation of spin-orbit materials using spin Peltier effect *Sci. Rep.* **8** 16067
[44] Qu D, Huang S Y, Guo G Y and Chien C L 2018 Inverse spin Hall effect in Au_xTa_{1-x} alloy films *Phys. Rev.* B **97** 024402
[45] Miao B F, Sun L, Wu D, Chien C L and Ding H F 2016 Magnetic scattering and spin-orbit coupling induced magnetoresistance in nonmagnetic heavy metal and magnetic insulator bilayer systems *Phys. Rev.* B **94** 174430
[46] Laczkowski P *et al* 2017 Large enhancement of the spin Hall effect in Au by side-jump scattering on Ta impurities *Phys. Rev.* B **96** 140405
[47] Zhang W *et al* 2016 Research update: spin transfer torques in permalloy on monolayer MoS_2 *APL Mater.* **4** 032302
[48] Jungfleisch M B *et al* 2016 Large spin-wave bullet in a ferrimagnetic insulator driven by the spin Hall effect *Phys. Rev. Lett.* **116** 057601
[49] Xu H *et al* 2020 High spin Hall conductivity in large-area type-II Dirac semimetal $PtTe_2$ *Adv. Mater.* **32** 2000513
[50] McMichael R D, Twisselmann D J and Kunz A 2003 Localized ferromagnetic resonance in inhomogeneous thin films *Phys. Rev. Lett.* **90** 227601
[51] Zakeri K *et al* 2007 Spin dynamics in ferromagnets: Gilbert damping and two-magnon scattering *Phys. Rev.* B **76** 104416
[52] Sun Y *et al* 2013 Damping in yttrium iron garnet nanoscale films capped by platinum *Phys. Rev. Lett.* **111** 106601
[53] Conca A, Heinz B, Schweizer M R, Keller S, Papaioannou E T and Hillebrands B 2017 Lack of correlation between the spin-mixing conductance and the inverse spin Hall effect generated voltages in CoFeB/Pt and CoFeB/Ta bilayers *Phys. Rev.* B **95** 174426
[54] Sato N, O'Brien K P, Millard K, Doyle B and Oguz K 2016 Investigation of extrinsic damping caused by magnetic dead layer in Ta-CoFeB-MgO multilayers with perpendicular anisotropy *J. Appl. Phys.* **119** 093902
[55] Shaw J M, Nembach H T and Silva T J 2012 Determination of spin pumping as a source of linewidth in sputtered Co 90Fe 10/Pd multilayers by use of broadband ferromagnetic resonance spectroscopy *Phys. Rev.* B **85** 054412
[56] Brataas A, Kent A D and Ohno H 2012 Current-induced torques in magnetic materials *Nat. Mater.* **11** 372–81
[57] Nakayama H *et al* 2013 Spin Hall magnetoresistance induced by a nonequilibrium proximity effect *Phys. Rev. Lett.* **110** 206601
[58] Elliott R J 1954 Theory of the effect of spin-orbit coupling on magnetic resonance in some semiconductors *Phys. Rev.* **96** 266–79
[59] Yafet Y 1961 Hyperfine interaction due to orbital magnetic moment of electrons with large g factors *J. Phys. Chem. Solids* **21** 99–104
[60] Marmion S R, Ali M, McLaren M, Williams D A and Hickey B J 2014 Temperature dependence of spin Hall magnetoresistance in thin YIG/Pt films *Phys. Rev.* B **89** 220404

[61] Ma L *et al* 2016 Spin orbit coupling controlled spin pumping and spin Hall magnetoresistance effects *Adv. Electron. Mater.* **2** 1600112
[62] Zhang W, Han W, Jiang X, Yang S H and Parkin S S P 2015 Role of transparency of platinum-ferromagnet interfaces in determining the intrinsic magnitude of the spin Hall effect *Nat. Phys.* **11** 496–502
[63] Panda S N, Mondal S, Sinha J, Choudhury S and Barman A 2019 All-optical detection of interfacial spin transparency from spin pumping in β-Ta/CoFeB thin films *Sci. Adv.* **5** eaav7200
[64] Pai C-F, Ou Y, Vilela-Leão L H, Ralph D C and Buhrman R A 2015 Dependence of the efficiency of spin Hall torque on the transparency of Pt/ferromagnetic layer interfaces *Phys. Rev.* B **92** 064426
[65] Lee K-M, Choi J W, Sok J and Min B-C 2017 Temperature dependence of the interfacial magnetic anisotropy in W/CoFeB/MgO *AIP Adv.* **7** 065107
[66] Phu P, Yamanoi K, Ohnishi K, Hyodo J, Rogdakis K, Yamazaki Y, Kimura T and Kurebayashi H 2019 Bolometric ferromagnetic resonance techniques for characterising spin-Hall effect at high temperatures *J. Magn. Magn. Mater.* **485** 304–7
[67] Fähnle M and Illg C 2011 Electron theory of fast and ultrafast dissipative magnetization dynamics *J. Phys.: Condens. Matter* **23** 493201
[68] Lu G, Huang X, Fan S, Ling W, Liu M, Li J, Jin L and Pan L 2018 Temperature-and thickness -dependent dynamic magnetic properties of sputtered CoFeB/Ta bilayer films *J. Alloys Compd.* **753** 475–82
[69] Isasa M, Villamor E, Hueso L E, Gradhand M and Casanova F 2015 Temperature dependence of spin diffusion length and spin Hall angle in Au and Pt *Phys. Rev.* B **91** 024402
[70] Chen W, Xiao G, Zhang Q and Zhang X 2018 Temperature study of the giant spin Hall effect in the bulk limit of β- W *Phys. Rev.* B **98** 134411
[71] Niimi Y, Morota M, Wei D H, Deranlot C, Basletic M, Hamzic A, Fert A and Otani Y 2011 Extrinsic spin Hall effect induced by iridium impurities in copper *Phys. Rev. Lett.* **106** 126601